

1 Snow depth derived from Sentinel-1 compared to in-situ 2 observations in northern Finland

3 Adriano Lemos¹, Aku Riihelä¹

4 ¹ Finnish Meteorological Institute, Helsinki, Finland

5 *Correspondence to:* Adriano Lemos (adriano.lemos@fmi.fi)

6 Abstract

7

8 Seasonal snow in the northern regions plays an important role providing water resources for both consumption and
9 hydropower generation. Moreover, the snow changes in northern Finland during winter impact the local agriculture,
10 vegetation, tourism and recreational activities. In this study we estimated snow depth using an empirical methodology
11 applied to the dual-polarisation of the Sentinel-1 synthetic aperture radar (SAR) images and compared with in situ
12 measurements collected by automatic weather stations (AWS), and snow courses in northern Finland. We applied an adapted
13 version of the empirical methodology developed by Lievens et al. (2019) to retrieve snow depth, using Sentinel-1
14 constellation between 2019 and 2022, and then compared to measurements from three automatic weather stations available
15 over the same period. Overall, the Sentinel-1 snow depth retrievals were underestimated in comparison with the in-situ
16 measurements from the automatic weather stations. We found slightly different patterns for the different years, and an overall
17 correlation factor of 0.41, and a higher correlation in the 2020–2021 season ($R=0.52$). The high correlation between
18 estimated and measured snow depth at the Inari Nellim location ($R=0.81$) reinforces the potential ability to derive snow
19 changes in regions where in situ measurements of snow are currently lacking. Further investigation is still necessary to better
20 understand how the physical properties of the snowpack influence the backscatter response over shallow snow regions.

21

22 1 Introduction

23

24 Snow variations play an important role in the northern regions, providing water resources for both consumption and
25 hydropower generation. Seasonal snow variations in northern Finland during winter impact the local agriculture, vegetation,
26 tourism and recreational activities (Lehtonen et al., 2013; Luomaranta et al., 2019). Some regions in the Arctic are
27 experiencing a shortening in the snow cover duration during the past decades, and future projections demonstrate an increase
28 in the surface temperature and a continuous decrease of snow cover through time for the northern regions of Finland
29 (Lehtonen et al., 2013; Luomaranta et al., 2019). Thus, extensive monitoring of snow depth is crucial for various purposes.

30

31 Different measurements efforts play an important role in monitoring snow depth, including the Automatic Weather Stations
32 (AWS; Luomaranta et al., 2019), light detection and ranging (LiDAR) flights (Painter et al., 2016), and snow course
33 measurements (Leppänen et al., 2016). The collection of these data provides valuable and accurate measurements. However,
34 their spatiotemporally limited coverage restricts systematic monitoring. On the other hand, remote sensing techniques, such
35 as satellite observations and modelling, are key to improve the monitoring of snow over large areas all year around (Tsai et
36 al., 2019; Awasthi & Varade, 2020; Tsang et al., 2022). Satellites equipped with passive microwave radiometry sensors,
37 supported by the in situ measurements, have been extensively used to estimate snow water equivalent (SWE), the total water
38 content in the snowpack, for decades (Takala et al., 2011; Pulliainen et al., 2020). However, despite their daily temporal
39 resolution, the coarse spatial resolution (approximately 25 km by 25 km) and the dependency on the in-situ measurements
40 still impose some limitations on the use of passive microwave radiometry for snow cover monitoring.

41

42 Currently, several studies in shallow snow regions, where snow thickness is lower than 1 m, make use of the synthetic
43 aperture radar (SAR) measurements in the Ku-band ($\sim 12 - 18$ GHz), as well as the Ka-band ($\sim 26.5 - 40$ GHz), as these
44 frequencies are more sensitive to snow pack changes. However, the exact knowledge of the penetration depth of the SAR
45 signal in the snow pack still remains unknown and dependent on assumptions due to the snowpack characteristics, hindering
46 accurate assessments (Tsang et al., 2022; Jutila and Hass, 2023).

47

48 The use of Interferometric Synthetic Aperture Radar (InSAR) technique using the L-band ($\sim 1 - 2$ GHz) has shown promise,
49 as it operates at lower frequencies and is less affected by the presence of vegetation and dry snow (Ruiz et al., 2022).
50 However, the lack of freely available data makes its use more difficult. Future missions, such as the Radar Observing System
51 for Europe in L-band (ROSE-L), as well as the NASA-ISRO Synthetic Aperture Radar (NISAR), will provide freely
52 available L-band data worldwide, improving our understanding of snow changes and improving its monitoring capabilities.

53

54 The C-band backscatter measurements are widely used in several applications in the cryosphere. More specifically in the
55 context of snow research, previous studies explore the application of the SAR images to provide information of dry snow

56 accumulation (Bernier and Fortin, 1998), and evaluation of snowmelt dynamics in the alpine regions (Marin et al., 2020).
57 The behaviour of the C-band backscatter inside the snowpack is complex, and still an ongoing area of investigation
58 (Hoppinen et al., 2024). Previous studies show that backscatter variations during mid-winter for shallow snow regions are
59 dominated by the snow-ground interface and the dielectric constant of the soil, minimising the effect of the dry snowpack
60 (Sun et al., 2015). However, minimal changes in the snow microstructure, and in the water liquid content in the snowpack,
61 impacts the surface and volume scattering of the snow (Lievens et al., 2019, 2022). —Despite some challenges and
62 limitations, the use of the C-band (5 – 6 GHz) synthetic aperture radar images have demonstrated the ability to estimate snow
63 depth and provide valuable information about snow depth variations using the Sentinel-1 (S1) constellation (Lievens et al.,
64 2019, 2022; Dunmire et al., 2024; Hoppinen et al, 2024). They demonstrated the sensitivity of the co- and cross-polarised
65 backscatter observations from the S1Sentinel-1 satellites to estimate snow depth over mountainous regions in the Northern
66 Hemisphere, where the snow thickness exceeds 1 m. These findings open the potential and significance of the use of the
67 Sentinel-1 SAR images archive to estimate snow depth variation.

68

69 Snow depth estimates with high spatio-temporal resolution can improve our understanding of seasonal snow mass in
70 complex access areas. Thus, the objective of this study is to expand the use of the empirical methodology applied to
71 synthetic aperture radar images (Lievens et al., 2019) to estimate seasonal snow depth variations over shallow snow regions,
72 in northern Finland. The findings will then be compared with independent in situ measurements collected by automatic
73 weather stations (AWS), and snow courses, in the same area.

74

75

76 2 Data and methods

77

78 Study Area

79

80 The study area is located in the northern region of Finland, between the latitudes 68.3° and 69.3°N (Figure 1). The study area
81 has a relatively flat topography, ranging approximately between 100 m to 500 m in elevation. The snow depth (SD)
82 fluctuation is influenced by the variation of the local surface air temperature and precipitation (Luomaranta et al., 2019). In
83 the northern part from 1961–2014 the average snow depth during winter was 82.7 cm, and maximum snow depth reached
84 121.5 cm in 2000 (Luomaranta et al., 2019). Due to its proximity, the temperature variations in Northern Finland have a
85 strong influence of the Arctic Ocean (Aalto et al., 2016). The mean surface temperature in the north during the winter from
86 1988–2014 was -11.1°C, and average maximum surface temperatures reached approximately -7.2°C during the winter for the
87 same period (Luomaranta et al., 2019).

88

89 Automatic weather stations

90

91 In order to compare and evaluate the snow depth estimates derived from ~~S1~~~~Sentinel-1~~, we used snow depth and surface air
92 temperature measurements from three automatic weather stations (AWS), managed by the Finnish Meteorological Institute.
93 The snow depths are measured by the Campbell Scientific SR50AH instruments mounted on the stations, and the instrument
94 accuracy, according to the manufacturer, is approximately 1 cm. We extracted information of daily snow depth and surface
95 air temperature, spanning from 2019 to 2022, from the Finnish stations database around the Inari Lake (IL) region. The
96 ~~available~~~~chosen~~ the AWS's, followed by their respective locations (Figure 1), ~~elevation in meters above sea level (m.a.s.l.),~~
97 ~~and percentage of forest cover (FC) extracted from the Multi-source National Forest Inventory Raster Maps of 2021~~
98 ~~described below~~) are; Inari Nellim (IN - 68.849°N, 28.399°E, 121 m.a.s.l., 33% of FC), Inari Kaamanen (IK - 69.141°N,
99 27.266°E, 158 m.a.s.l., 26% of FC), and Inari Angeli Lintupuoliselkä (IA - 68.903°N, 25.736°E, 240 m.a.s.l., 24% of FC).

100

101 Snow courses

102

103 There are approximately 140 snow courses across Finland. Snow course measurements are operated, and provided, by the
104 Finnish Environment Institute (SYKE). Systematic measurements have been made, for some locations, by SYKE and the
105 Finnish Meteorological Institute (FMI) since the 1930s (Leppänen et al., 2016). Typically, each snow course is 2 to 4
106 kilometers long, measured in the middle of each month, and at about 80 regularly spaced points, usually every 50 meters
107 along the route (Leppänen et al., 2016). In this paper, we used averaged snow depth measurements along 6 snow courses
108 (Figure 1); Inari Nellim (IN - 68.849°N, 28.399°E), Inari Angeli Lintupuoliselkä (IA - 68.903°N, 25.736°E), Inari
109 Mutusjärvi (IM - 68.961°N, 26.739°E), Inari Repojoki (IR - 68.450°N, 25.977°E), Inari Kaasmukka (IKa - 69.307°N,
110 26.656°E), and Inari Laanioja (IL - 68.371°N, 27.453°E).

111

112

113 Canopy cover

114

115 We used the canopy cover from the Multi-source National Forest Inventory Raster Maps of 2021 (MS-NFI), which is
116 processed and distributed by the Luonnonvarakeskus (Natural Resources Centre) from Finland, to evaluate the correlation
117 with the snow depth patterns derived from ~~S1~~~~Sentinel-1~~. The main products used to derive the canopy cover, and the other
118 products distributed, are from the Sentinel-2A/B satellites of European Space Agency (ESA) and the Landsat 8 satellite of
119 United States Geological Survey (USGS), the full description of the data is found in Mäkisara et al. (2022). The dataset
120 comes in the ETRS-TM35FIN coordinate system, and the spatial resolution is posted at 16 m by 16 m. Areas affected by
121 cloud coverage, regions outside forest land, and outside Finland are removed and disregarded (Mäkisara et al., 2022).

122

123 Sentinel-1 data

124

125 In this study we estimated snow depth using single look complex (SLC) synthetic aperture radar images acquired in the
126 interferometric wide swath (IW) mode from the ~~S1Sentinel-1~~ satellite launched by the European Space Agency (ESA) in
127 October 2014. Sentinel-1b was launched in April 2016 and ended its mission in December 2021 due to technical issues. For
128 this reason, in the present work, we preferred to use only images acquired from Sentinel-1a, and referred from here as
129 ~~S1Sentinel-1~~. The Sentinel SAR instruments operate at C-band (5.405 GHz), and the IW mode has a 250 km swath and
130 spatial resolution of 5 m in ground range and 20 m in azimuth. Each satellite from the ~~S1Sentinel-1~~ constellation had a repeat
131 cycle of 12 days and 180 degrees orbital phasing difference. We used the dual-polarisation (VH and VV) components from
132 56 SAR ~~S1Sentinel-1~~ images acquired over the same region in northern Finland. The data range acquired spans from
133 October 2019 to May 2022 (Table S1 in the Supplementary data), and we followed the workflow described below to derive
134 56 snow depth maps.

135

136 In the pre-processing stage we used ESA's Sentinel Applications Platform (SNAP) software (version 8.0). We performed a
137 standard processing routine for all the ~~S1Sentinel-1~~ SLC IW images, including the application of the most recent orbit file,
138 radiometric calibration, debursting and range-Doppler terrain correction using the Copernicus digital elevation model (DEM)
139 posted to a spatial resolution grid of 30 m. Previous studies showed that speckle noise makes the data product more variable,
140 and the upscaling of the S1 data has presented better snow depth estimates (Lievens et al., 2022; Dunmire et al., 2024;
141 Hoppinen et al., 2024). In order to reduce speckle noise in the SAR measurements, we applied a moving mean filter to the
142 data, using a kernel of 990 m by 990 m. The final pre-processed product was a time-series of stacked S1 images with σ^0
143 backscatter intensities in decibel (dB) for both HV and VV.

144

145 We used an adapted version of the empirical methodology developed by Lievens et al. (2019) to estimate snow depth using
146 ~~S1Sentinel-1~~ products (Equations 1 and 2). The algorithm utilises changes in the cross-polarized backscatter measurements
147 of SAR images repeatedly acquired on the same location and orbit to avoid geometry distortions. We calculated the ratio
148 between the two cross-polarised (σ_{vh}^0 and σ_{vv}^0) backscatter intensities (in dB) in a pixel scale for the entire image time-series.
149 We considered the entire region as susceptible to snow accumulation, and the snow index (SI) in the time step t_i , was
150 calculated as described in the Equation (1). Moreover, if $SI(t_i) < 0$, it was considered as zero.

151

$$152 \quad SI(t_i) = SI(t_{i-1}) + [(\sigma_{vh}^0 / \sigma_{vv}^0)(t_i) - (\sigma_{vh}^0 / \sigma_{vv}^0)(t_{i-1})] \quad (\text{Equation 1})$$

153

154 The translation to snow depth (SD), in metres, is then calculated using Equation 2.

155

$$SD(t_i) = \left(\frac{a}{1 - bFC(i)} \right) SI(t_i) \quad (\text{Equation 2})$$

157

158 The parameter $a=1.1 \text{ m dB}^{-1}$ (Equation 2) is constant and was estimated using in situ measurements, minimising the mean
 159 absolute error (MAE) between the times series of the global average snow depth measurements and ~~S1Sentinel-1~~ estimates
 160 in mountain regions (Lievens et al., 2019). The forest cover (FC) used here is the canopy cover from the Multi-source
 161 National Forest Inventory Raster Maps of 2021 (MS-NFI). As the canopy cover attenuates the backscatter from the snow, an
 162 additional parameter $b=0.6$ (dimensionless), estimated by Lievens et al. (2019), is applied.

163

164 Errors in our snow depth estimates arise mainly through the radiometric accuracy for ~~S1Sentinel-1~~, specified as $\sim 1 \text{ dB}$
 165 (Torres et al., 2012). Due to the fact we averaged all the σ^0 images to reduce speckle, an additional 0.5 dB was considered
 166 into the overall radiometric accuracy (Torres et al., 2012). The resulting radiometric accuracy of 1.5 dB , representing
 167 $\sim 10\text{-}15\%$ of the σ^0 signal, was used to determine the uncertainty of the snow depth measurements.

168

169

170 3 Results and Discussions

171

172 We used the ~~S1Sentinel-1~~ dataset (Table S1) between 2019–2022 to produce up-to-date snow depth at our designated study
 173 area (Figure 1). To explore changes in snow depth over space and time, we further extracted time series of snow depth to
 174 compare them to independent measurements from the three automatic weather stations (Figure 2). Then, we show mean
 175 snow depths yearly in Figure 3. Figure 4 presents the snow depth estimates separated by canopy density intervals.
 176 Furthermore, in order to evaluate the snow depth estimates from S1, the dataset was compared to the automatic weather
 177 stations in different scenarios, presented in the Figures 5 and 6.

178

179 Figure 2 displays the seasonal changes in the snow depth over three consecutive winters at the AWS sites. We observe that
 180 the snow depth estimates from S1 at the Inari Nellim location (Figure 2a) follows the seasonal variations measured by the
 181 automatic weather stations measurements, despite the underestimated values. The snow depth products derived from
 182 ~~S1Sentinel-1~~ from the other weather stations, IK and IA (Figures 2b and 2c), also follow the seasonality of the weather
 183 stations measurements, although they exhibit an evident underestimation relative to the AWS measurements. Automatic
 184 weather stations are usually located in relatively flat and non-forested terrain, which may not accurately represent the
 185 surrounding area, susceptible to changes in e.g., forest cover and terrain. Thus, it is important to highlight the challenges
 186 when comparing observations from a point-scale measurement from the AWS's, and the grid-scale estimates from
 187 ~~S1Sentinel-1~~ (Lievens et al., 2022). For this purpose, we compared the snow depth estimates from S1 to average snow depth

188 measured (Figure S3) along the snow courses at 6 locations (Figure 1) available for the region. Overall, we observed clear
189 underestimations in the shallow snow depth estimates regions (Figure 2 and S3), in agreement with Lievens et al. (2019).
190 Theoretically, the underestimation is possibly due to the water content in the snowpack, reflecting and absorbing the
191 backscatter signal, as the ground temperature in the accumulation period remains approximately the same, insulated by the
192 snow (Lievens et al., 2019; Marin et al., 2020). The mean snow depths from S1 estimates are ~20.0 cm, ~10.1 cm, and ~13.4
193 cm, for Inari Nellim, Inari Kaamanen, and Inari Angeli L. locations respectively (Table 1). In contrast, the mean snow depth
194 measured by the automatic weather stations IN, IK and IA are, respectively, ~37.1 cm, ~46.9 cm, and ~44.9 cm (Table 1).
195 We notice from Figure S1, presenting the bias evolution of the snow depth as a function of the days of the year, that the snow
196 season onset is well estimated by the method, despite the rapid bias increase as the snow season progresses.

197

198 The maps in Figures 3 present the average snow depth along the years. Overall, we find higher mean snow depth estimates in
199 2019–2020 (Figure 3a), following the AWS's measurements from the time series in Figure 2 during the same year.
200 Furthermore, we noticed higher mean snow thickness over water bodies regions, reaching values over 50 cm for all the
201 estimates along the years (Figure 3). In order to compare the snow thickness estimates from S1 Sentinel-1, we plotted the
202 snow depth measured in snow pits (sp1-4 in Figure 1) during a field campaign around the Inari Lake region from the 3rd to 7th
203 of April 2022 against the estimates 6th of April 2022 from S1 (Figure S2), as this is the closest estimate to the field
204 measurements. We observe that, in comparison with the snow pits measurements on the lake region, all the snow depth
205 derived from S1 are overestimated (Figure S1). Moreover, visually comparing the backscatter signal from the co- and cross-
206 polarizations, VV and VH respectively, from S1 (Figures S43 and S54), we can observe that the VV component
207 demonstrates to be more sensitive when the lake starts freezing, around 11th November. The backscatter signal increases
208 (Figures S43 and S54), leading to an increase in the snow depth values.

209

210 Forest areas attenuate the radar waves, scattering the emitted and the received signal from the satellite to the snow cover on
211 the ground, and vice-versa, leading to an underestimation of the results (Lievens et. al, 2019; Tsang et al., 2022). In order to
212 investigate the influence of the forest cover, we divided the canopy density map (Figure 4a), from Multi-source National
213 Forest Inventory Raster Maps of 2021, into forest cover density intervals and calculated the mean snow depth for each
214 interval yearly (Figure 4b). We observe for all the years, and overall mean, thicker snow depth values over dense vegetation
215 (50-100% of canopy coverage) and water bodies areas, where the canopy density is equal to 0% (Figure 4b). The mean snow
216 depth from the year 2021-2022 (red bars in Figure 4) presents a slight snow depth decrease where the canopy density is
217 above 40%. For the 2019-2020 and 2020-2021 years, we found thicker snow layers over denser canopy regions (orange and
218 green bars in Figure 4b, respectively). Despite the aligned increase of snow thickness and canopy density, the estimated snow
219 depth over the forested areas are underestimated if compared to the automatic weather stations (Figure 2). Figure 45b shows
220 a maximum snow depth of ~57 cm (canopy density over 20%) in 2019-2020, and a maximum snow depth of ~37 cm for the
221 remaining years. Similar results were found using L-band SAR images, showing that the snow depth variations over the

222 forested areas are also underestimated compared to vegetation free regions (Ruiz et al., 2022). It is important to comment
223 that we also utilised the same approach described before (Figure 4) to correlate our snow depth estimates with terrain
224 elevation intervals. We divided the digital elevation model in intervals every 100 m, going up to its maximum (~500 m).
225 However, we have not found any significant correlation to include in this manuscript.

226

227 In order to compare the S1 estimates and the AWS's measurements, we calculated the temporal correlation coefficients in
228 two different scenarios (Figs. 5 and 6). In the first scenario (Sc1) we considered all the measurements at once, as well as
229 separated AWS's locations (Figure 5). In the second scenario (Sc2), we looked at individual years separately (Figure 6).
230 Figure 5 displays the overall correlation, Sc1, using all the 174 measurements for all the years and from the three sites. It
231 presented a low correlation of 0.41 and a mean absolute error of ~26.1 cm (Table 2). The estimates at the Inari Nellim
232 weather station had a high correlation of 0.81, when compared with the other locations with $R=0.09$ and $R=0.55$ for Inari
233 Kaamanen and Inari Angeli locations, respectively (Figure 5). Figure 6 presents all the 174 measurements separated yearly.
234 We observe that the year 2020–2021 had the higher correlation factor, $R = 0.52$, as well as the smaller mean absolute error
235 (~15 cm; Table 2). The years 2019–2020 and 2021–2022 presented correlation factors of 0.29 for both years (Figure 6), and
236 mean absolute errors of ~38.9 cm and ~25.5 cm, respectively (Table 2).

237

238 The uncertainty in the AWS snow depth observations (~1 cm) is considerably smaller than the uncertainty of the SAR-based
239 estimates due to radiometric noise in the SAR imagery. At the Nellim site, a considerable part of the bias between the
240 SAR-based estimate and ground truth could be explained by the estimation uncertainty, yet the same does not hold for either
241 Kaamanen or Angeli. We thus conclude that the observed underestimation should be considered significant in relation to the
242 uncertainty of the estimation method.

243

244 The backscatter signal from co-polarised images in the C-band on dry snow conditions is strongly influenced by the ground
245 underneath, and by the water content in the snowpack (Sun et al., 2015; Marin et al., 2020; Feng et al., 2021; Lievens et al.,
246 2022). ERS and Radarsat, both in the C-band, demonstrated an increase in the co-polarised backscatter signal during the
247 snow accumulation periods (Bernier and Fortin, 1998) and a decrease over shallow areas (Rott and Nagler, 1993). Following
248 the same empirical hypothesis demonstrated by Lievens et al. (2019) and Lievens et al. (2022), the cross-polarised
249 backscatter signals at C-band are more responsive to dry snow accumulation, in comparison to the backscatter influence
250 from the ground. Lievens et al. (2019) suggest that dry snow is represented by layers of large clusters of irregular ice
251 crystals, scattering on the snow layer interfaces. Therefore, for deep snow locations, it is expected that layered snow
252 enhances and dominates the backscatter signal, from cross-polarised observations (Lievens, et al., 2019).

253

254 Given the considerable underestimation of snow depth over land, and conversely considerable overestimation of snow depth
255 over lake ice, our results reinforce the idea that the EM properties of the surface underlying the shallow seasonal snowpack

likely play a major role in the observable SAR backscatter. There is a clear need for dedicated studies to improve radiative transfer modelling of volume scattering of snow in order to better explain the observed behaviour, as pointed out by Lievens et al. (2019). Finally, it is worth pointing out that the backscatter ratios are converted into snow depth through empirical coefficients. While the calibration coefficients are based on a large number of data (Lievens et al., 2019), they are based on relationships observed for mountainous snow packs, and thus not necessarily valid for shallow snow packs elsewhere. Recalibration of the coefficients is not considered here due to the limited number of reference snow depth observation sites in our study area. We also point out that at Kaamanen in particular, the temporal evolution of the backscatter ratios would not have tracked the snow depth evolution even if other linear calibrations were attempted. This further points to a need for rigorous radiative transfer studies to better understand the composition of C-band SAR backscatter over seasonal shallow snowpacks.

4 Conclusions

We investigated the use of co- and cross-polarised backscatter from Sentinel-1 SAR C-band images ~~from the Sentinel-1 satellite~~ to estimate snow depth variations over the northern region of Finland from 2019 to 2022. We presented a high temporal resolution comparison between snow depth estimated from ~~S1~~~~Sentinel-1~~ images and measurements from automatic weather stations, and correlated with canopy cover provided by Luonnonvarakeskus (Natural Resources Institute of Finland). The use of the C-band SAR to estimate snow depth over shallow snow regions presented limitations. In general, we found underestimation for all the years and locations. It is important to highlight the snow depth estimates at the Inari Nellim location, which demonstrated the best results ($R=0.81$), when compared to the automatic weather station measurements at the same location. Looking throughout the years, the year 2020–2021 presented better results ($R=0.52$), when compared to the previous years.

We also investigated the correlation between the canopy coverage and the snow depth estimations, and we observed thicker snow depth values over dense vegetation and water bodies regions. These findings are possibly due to the high sensitivity of the VV component over freshly frozen water, increasing the backscatter significantly. We recognize that deriving shallow snow depths using C-band SAR images is still a challenge and further investigation is necessary to better understand the observed underestimation. Thanks to the effort of international space agencies, we have available currently, and will have in the near future, global coverage at high-temporal and -spatial resolution of SAR imagery. Combined with installed automatic weather stations, this opens the possibility of a wide spatial monitoring of snow variations independent of weather or solar illumination conditions. However, given the present under- and overestimations observed against reference snow depth data, we emphasise the first-order need for rigorous radiative transfer model-based studies to comprehensively understand the drivers of SAR backscatter from snowpacks.

290

291

292 *Data availability.* The dataset will be available on the METIS - Finnish Meteorological Institute Research Data repository.

293

294 *Competing interests.* The authors declare that they have no conflict of interest.

295

296 *Acknowledgements.* This work was supported by the Academy of Finland, under the project “Low orbit altimetry, albedo,
297 and Antarctic Snow and Sea-ice Surface Roughness” (LAS3R), grant number 335986. The authors gratefully acknowledge
298 the European Space Agency for the Copernicus Sentinel 1 data acquired from Data Hub, courtesy of the EU/ESA. The
299 Sentinel-1 data are freely available at <https://scihub.copernicus.eu/> (last access: 01 June 2023). The authors also
300 acknowledge Luonnonvarakeskus (Natural Resources Institute of Finland) to provide the National Forest Inventory Raster
301 Maps of 2021, and the Finnish Meteorological Institute for the automatic weather station datasets available at
302 <https://hav.fmi.fi> (last access: 02 February 2023). We acknowledge Pjnia Venäläinen and Kari Luojus for providing the snow
303 courses dataset. We thank the editor Ruth Mottram, and the two anonymous referees, for their comments, which helped to
304 improve the manuscript.

305

306 References

- 307 Aalto, J., Pirinen, P., and Jylhä, K.: New gridded daily climatology of Finland: Permutation-based uncertainty estimates and
308 temporal trends in climate, *J. Geophys. Res.*, 121, 3807–3823, <https://doi.org/10.1002/2015JD024651>, 2016.
- 309 Awasthi, S., & Varade, D. (2021). Recent advances in the remote sensing of alpine snow: a review. In *GIScience and Remote*
310 *Sensing* (Vol. 58, Issue 6, pp. 852–888). Taylor and Francis Ltd. <https://doi.org/10.1080/15481603.2021.1946938>.
- 311 Bernier, M. and Fortin, J. P.: The potential of time series of C-Band SAR data to monitor dry and shallow snow cover, *IEEE*
312 *Trans. Geosci. Remote Sens.*, 36, 226–243, <https://doi.org/10.1109/36.655332>, 1998.
- 313 Dunmire, D., Lievens, H., Boeykens, L., & de Lannoy, G. J. M. (2024). A machine learning approach for estimating snow
314 depth across the European Alps from Sentinel-1 imagery. *Remote Sensing of Environment*, 314,
315 <https://doi.org/10.1016/j.rse.2024.114369>.
- 316 Feng, T., Hao, X., Wang, J., Li, H., & Zhang, J. (2021). Quantitative evaluation of the soil signal effect on the correlation
317 between sentinel-1 cross ratio and snow depth. *Remote Sensing*, 13(22). <https://doi.org/10.3390/rs13224691>.
- 318 Hoppinen, Z., Palomaki, R. T., Brencher, G., Dunmire, D., Gagliano, E., Marziliano, A., Tarricone, J., & Marshall, H.-P.
319 (2024). Evaluating snow depth retrievals from Sentinel-1 volume scattering over NASA SnowEx sites. *The Cryosphere*,
320 18(11), 5407–5430. <https://doi.org/10.5194/tc-18-5407-2024>.
- 321 Lehtonen, I., Venäläinen, A., Ikonen, J., Puttonen, N., and Gregow, H.: Some features of winter climate in Northern
322 Fennoscandia, *Ilmatieteen Laitos Rap.*, 32, 2013.
- 323 Leppänen, L., Kontu, A., Sjöblom, H., and Pulliainen, J.: Sodankylä manual snow survey program, *Geosci. Instrum.*
324 *Methods Data Syst.*, 5, 163–179, <https://doi.org/10.5194/gi-5-163-2016>, 2016.
- 325 Lievens, H., Demuzere, M., Marshall, H. P., Reichle, R. H., Brucker, L., Brangers, I., de Rosnay, P., Dumont, M., Giroto,
326 M., Immerzeel, W. W., Jonas, T., Kim, E. J., Koch, I., Marty, C., Saloranta, T., Schöber, J., and De Lannoy, G. J. M.: Snow
327 depth variability in the Northern Hemisphere mountains observed from space, *Nat. Commun.*, 10,
328 <https://doi.org/10.1038/s41467-019-12566-y>, 2019.
- 329 Lievens, H., Brangers, I., Marshall, H. P., Jonas, T., Olefs, M., and De Lannoy, G.: Sentinel-1 snow depth retrieval at
330 sub-kilometer resolution over the European Alps, *Cryosphere*, 16, 159–177, <https://doi.org/10.5194/tc-16-159-2022>, 2022.
- 331 Luomaranta, A., Aalto, J., and Jylhä, K.: Snow cover trends in Finland over 1961–2014 based on gridded snow depth
332 observations, *Int. J. Climatol.*, 39, 3147–3159, <https://doi.org/10.1002/joc.6007>, 2019.

333 Marin, C., Bertoldi, G., Premier, V., Callegari, M., Brida, C., Hürkamp, K., Tschiersch, J., Zebisch, M., and Notarnicola, C.:
 334 Use of Sentinel-1 radar observations to evaluate snowmelt dynamics in alpine regions, *The Cryosphere*, 14, 935–956,
 335 <https://doi.org/10.5194/tc-14-935-2020>, 2020.

336 Painter, T. H., Berisford, D. F., Boardman, J. W., Bormann, K. J., Deems, J. S., Gehrke, F., Hedrick, A., Joyce, M., Laidlaw,
 337 R., Marks, D., Mattmann, C., McGurk, B., Ramirez, P., Richardson, M., Skiles, S. M. K., Seidel, F. C., and Winstral, A.: The
 338 Airborne Snow Observatory: Fusion of scanning lidar, imaging spectrometer, and physically-based modelling for mapping
 339 snow water equivalent and snow albedo, *Remote Sens. Environ.*, 184, 139–152, <https://doi.org/10.1016/j.rse.2016.06.018>,
 340 2016.

341 Pulliainen, J., Luojus, K., Derksen, C., Mudryk, L., Lemmetyinen, J., Salminen, M., Ikonen, J., Takala, M., Cohen, J.,
 342 Smolander, T., and Norberg, J.: Patterns and trends of Northern Hemisphere snow mass from 1980 to 2018, *Nature*, 581,
 343 294–298, <https://doi.org/10.1038/s41586-020-2258-0>, 2020.

344 Ruiz, J. J., Lemmetyinen, J., Kontu, A., Tarvainen, R., Vehmas, R., Pulliainen, J., and Praks, J.: Investigation of
 345 Environmental Effects on Coherence Loss in SAR Interferometry for Snow Water Equivalent Retrieval, *IEEE Trans. Geosci.*
 346 *Remote Sens.*, 60, 1–15, <https://doi.org/10.1109/TGRS.2022.3223760>, 2022.

347 Sun, S., Che, T., Wang, J., Li, H., Hao, X., Wang, Z., & Wang, J. (2015). Estimation and analysis of snow water equivalents
 348 based on C-band SAR data and field measurements. *Arctic, Antarctic, and Alpine Research*, 47(2), 313–326.
 349 <https://doi.org/10.1657/AAAR00C-13-135>.

350 Takala, M., Luojus, K., Pulliainen, J., Derksen, C., Lemmetyinen, J., Kärnä, J. P., Koskinen, J., and Bojkov, B.: Estimating
 351 northern hemisphere snow water equivalent for climate research through assimilation of space-borne radiometer data and
 352 ground-based measurements, *Remote Sens. Environ.*, 115, 3517–3529, <https://doi.org/10.1016/j.rse.2011.08.014>, 2011.

353 Torres, R., Snoeij, P., Geudtner, D., Bibby, D., Davidson, M., Attema, E., Potin, P., Rommen, B., Floury, N., Brown, M.,
 354 Traver, I. N., Deghaye, P., Duesmann, B., Rosich, B., Miranda, N., Bruno, C., L’Abbate, M., Croci, R., Pietropaolo, A.,
 355 Rostan, F. (2012). GMES Sentinel-1 mission. *Remote Sensing of Environment*, 120, 9–24.
 356 <https://doi.org/10.1016/j.rse.2011.05.028>.

357 Tsai, Y. L. S., Dietz, A., Oppelt, N., & Kuenzer, C. (2019). Remote sensing of snow cover using spaceborne SAR: A review.
 358 In *Remote Sensing* (Vol. 11, Issue 12). MDPI AG. <https://doi.org/10.3390/rs11121456>.

359 Tsang, L., Durand, M., Derksen, C., Barros, A., Kang, D.-H., Lievens, H., Marshall, H.-P., Zhu, J., Johnson, J., King, J.,
 360 Lemmetyinen, J., Sandells, M., Rutter, N., Siqueira, P., Nolin, A., Osmanoglu, B., Vuyovich, C., Kim, E., Taylor, D.,
 361 Merkouriadi, I., Brucker, L., Navari, M., Dumont, M., Kelly, R., Kim, R. S., Liao, T.-H., and Xu, X.: Review Article: Global

362 Monitoring of Snow Water Equivalent using High Frequency Radar Remote Sensing, *The Cryosphere*, 16, 3531–3573,
363 <https://doi.org/10.5194/tc-2021-295>, 2022.

364

365

366

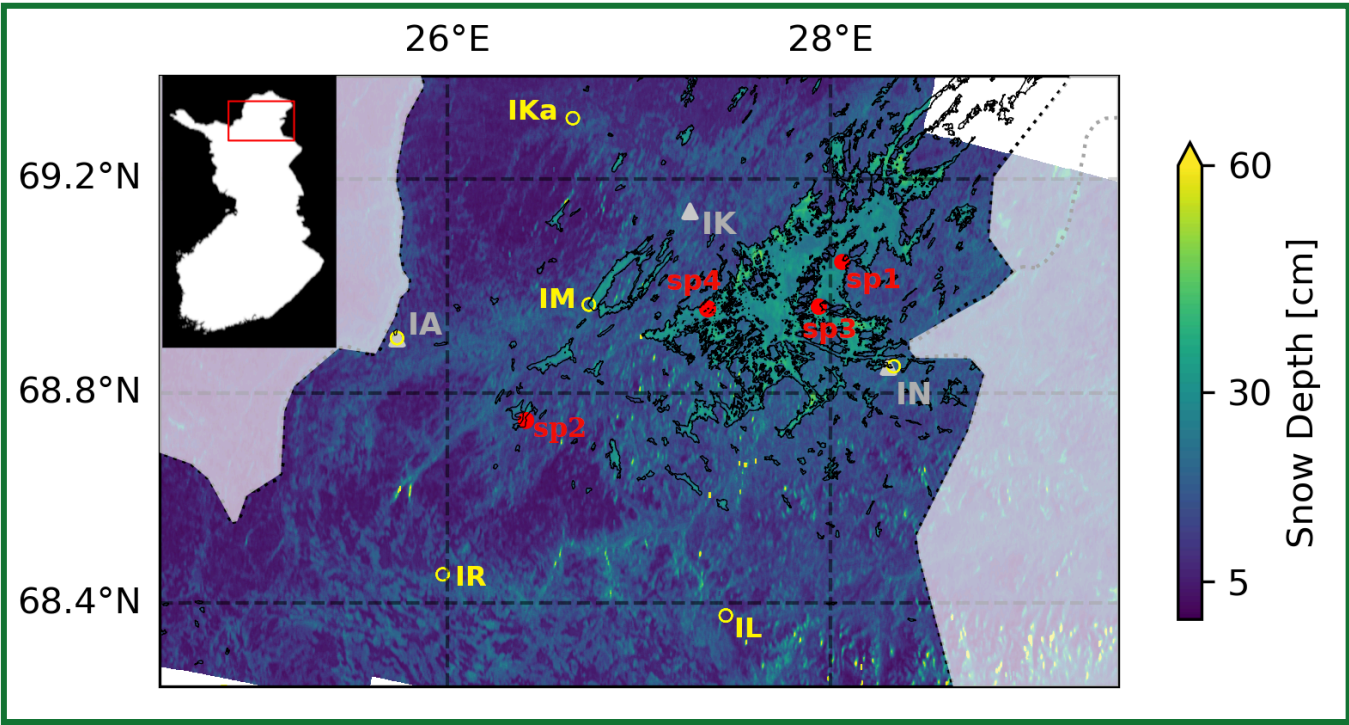
367 **Figures**

368

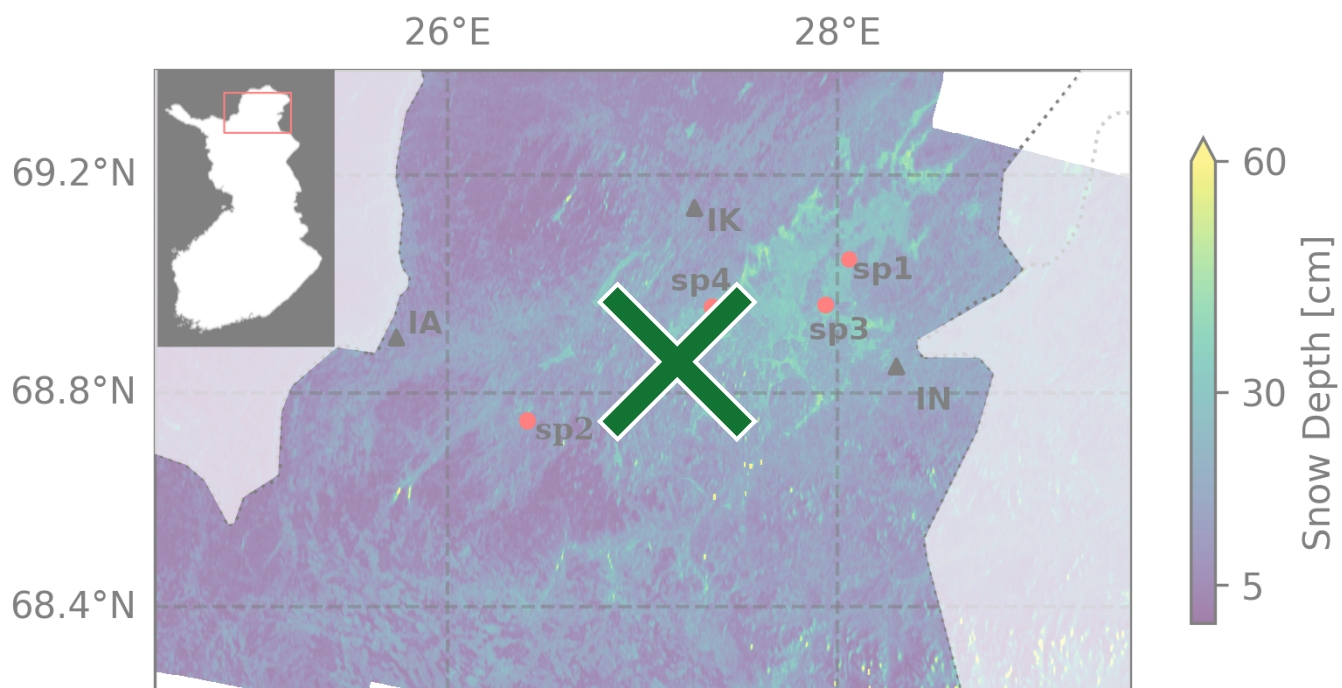
369 Figure 1: Average snow depth estimated from ~~S1~~**Sentinel-1** between 2019–2022 (between October and March). Black
370 triangles indicate the automatic weather stations' locations; Inari Nellim (IN), Kaamanen (IK), and Angeli Lintupuoliselkä
371 (IA), respectively. The red dots are representing the snow pits measurements (sp1–sp4). **Yellow circles are the snow course**
372 **locations; Inari Angeli Lintupuoliselkä (IA), Inari Kaasmukka (IKa), Inari Laanioja (IL), Inari Mutusjärvi (IM), Inari**
373 **Nellim (IN), and Inari Repojoiki (IR).** The inset figure shows the study region in Finland.

374

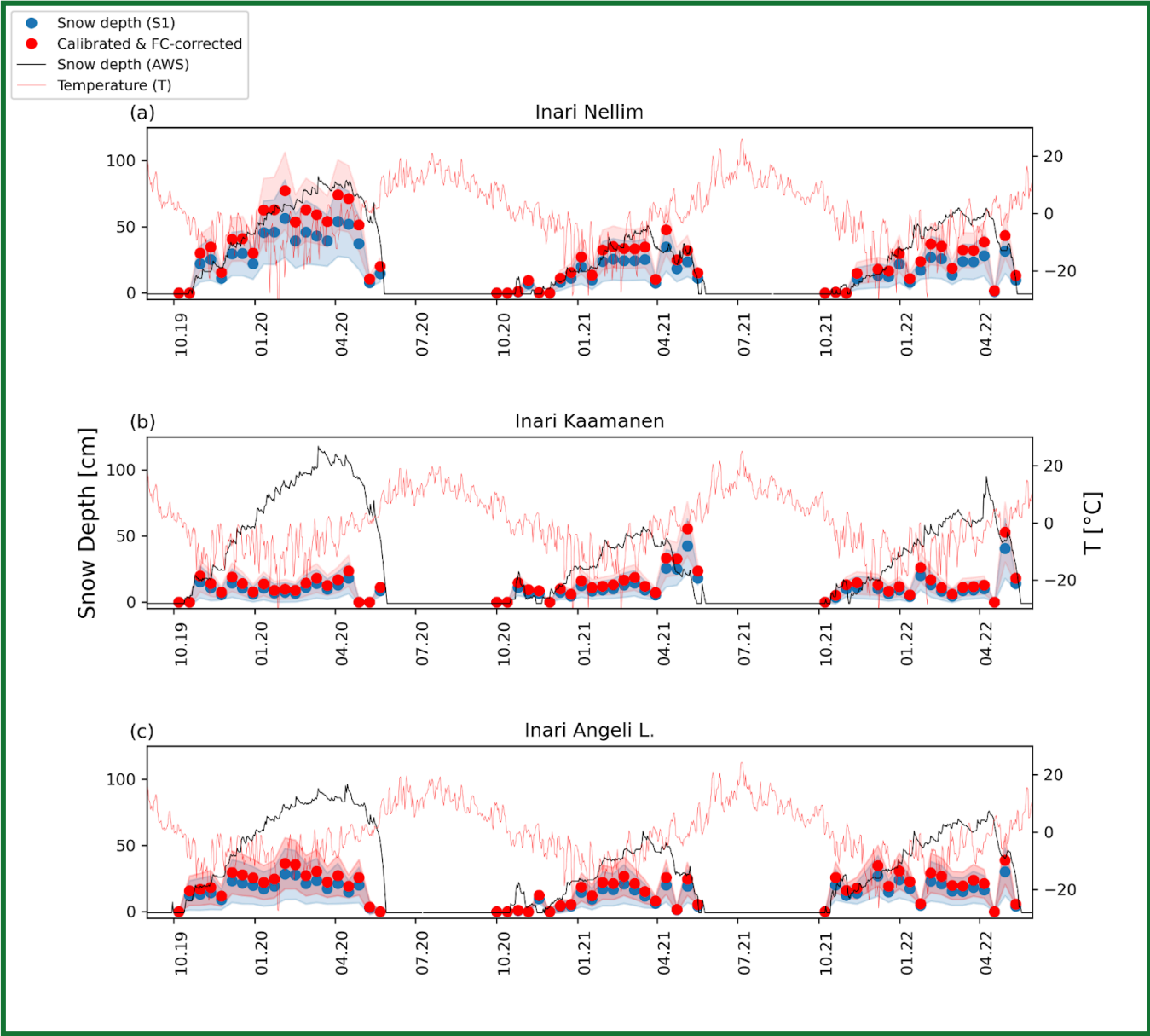
375



376
377



378 Figure 2: Snow depth variation between 2019 and 2022. The blue dots represent the snow depth variation estimated from the
 379 S1 images before the correction done due the calibration and forest cover (FC) attenuation. Corrected values are represented
 380 by the red dots. The uncertainty ranges are represented by the light blue and red shading. On the left y-axis, the solid black
 381 line represents snow depth from the automatic weather stations and the blue dots are snow depth estimates derived by
 382 S1 Sentinel-1. On the right y-axis, the solid red lines represent surface temperature daily averaged respectively.
 383



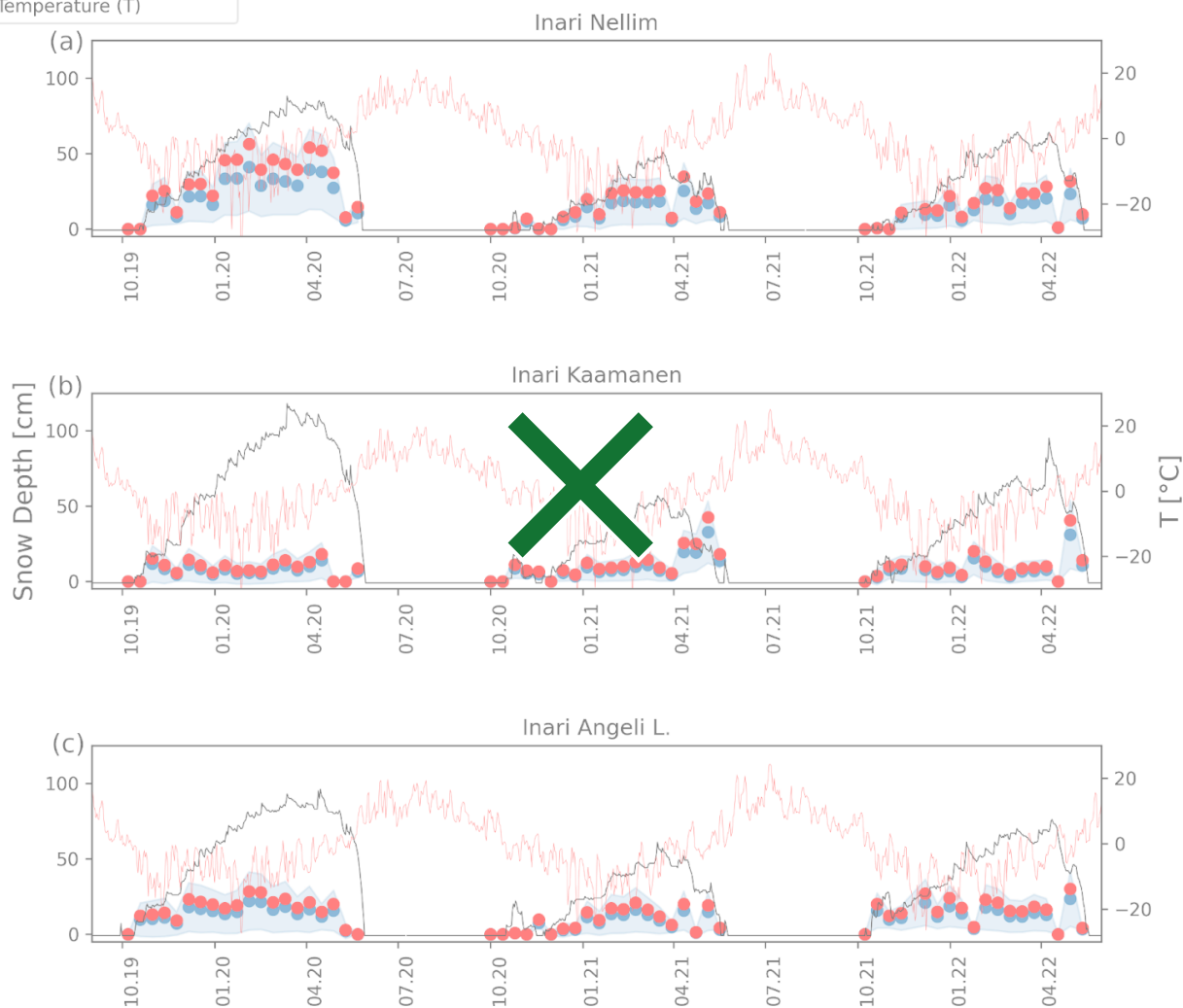
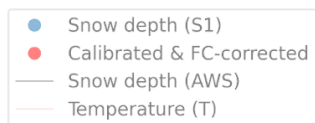
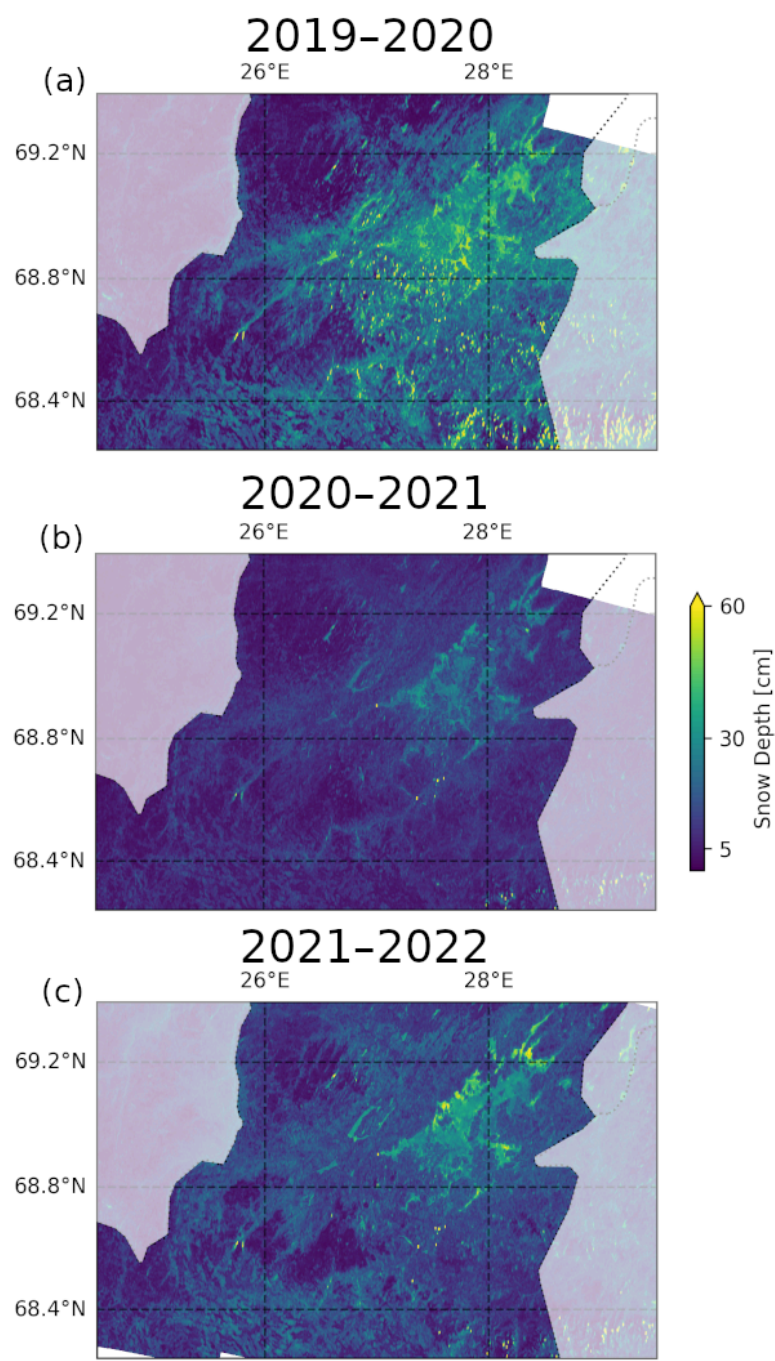
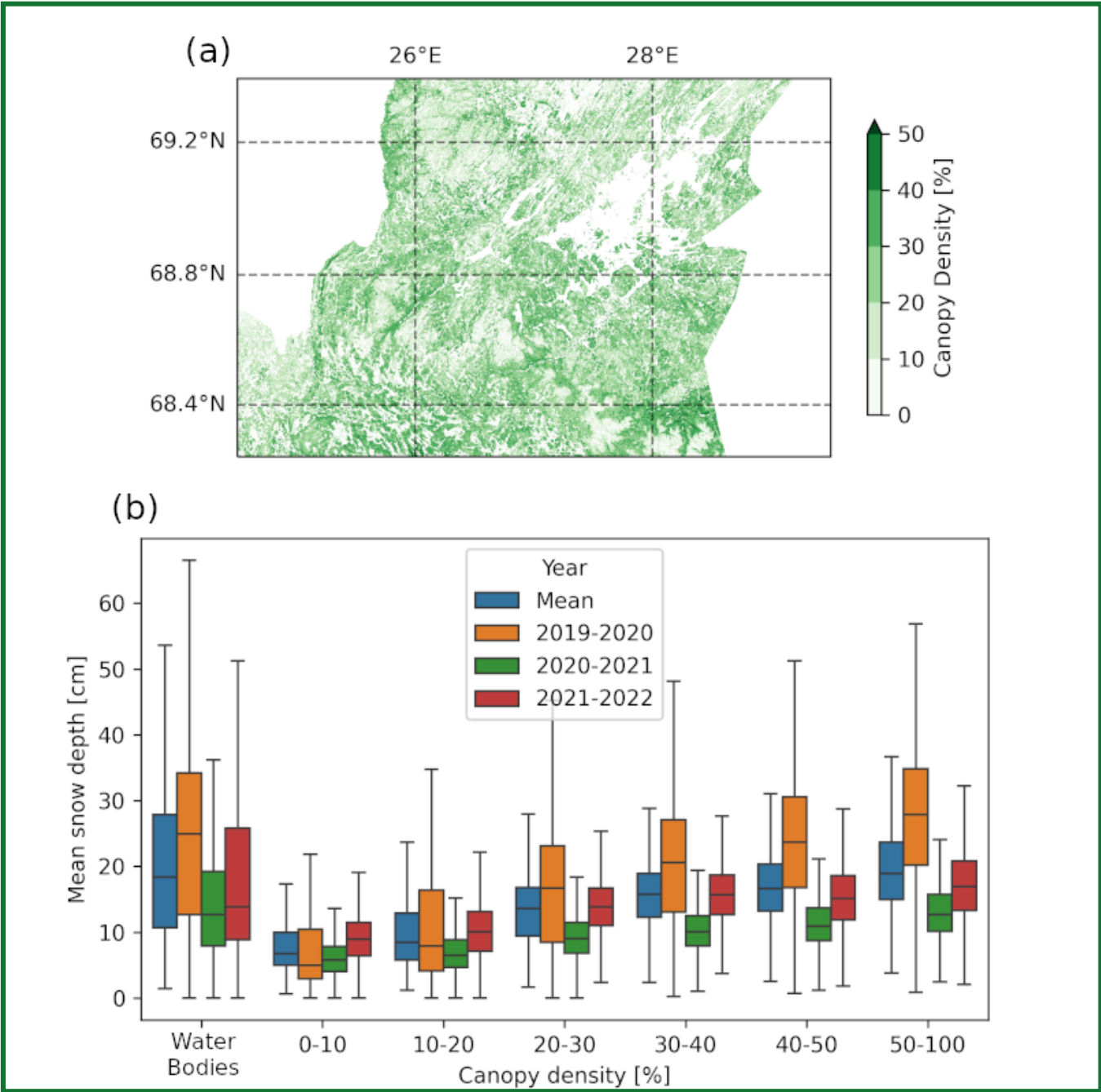


Figure 3: Average snow depth estimated from Sentinel-1 during the years of 2019–2020 (a), 2020–2021 (b), and 2021–2022 (c), respectively.



391 Figure 4: Canopy density map represented from 2021 (a). Mean snow depth separated in different canopy density intervals
 392 (b). The bottom and top of the vertical boxes represent the 25th and 75th interquartile, respectively. The solid black line
 393 inside the boxes represents the median snow depth estimate for each interval. Values outside the whiskers' extent are not
 394 shown and they are statistically considered outliers.



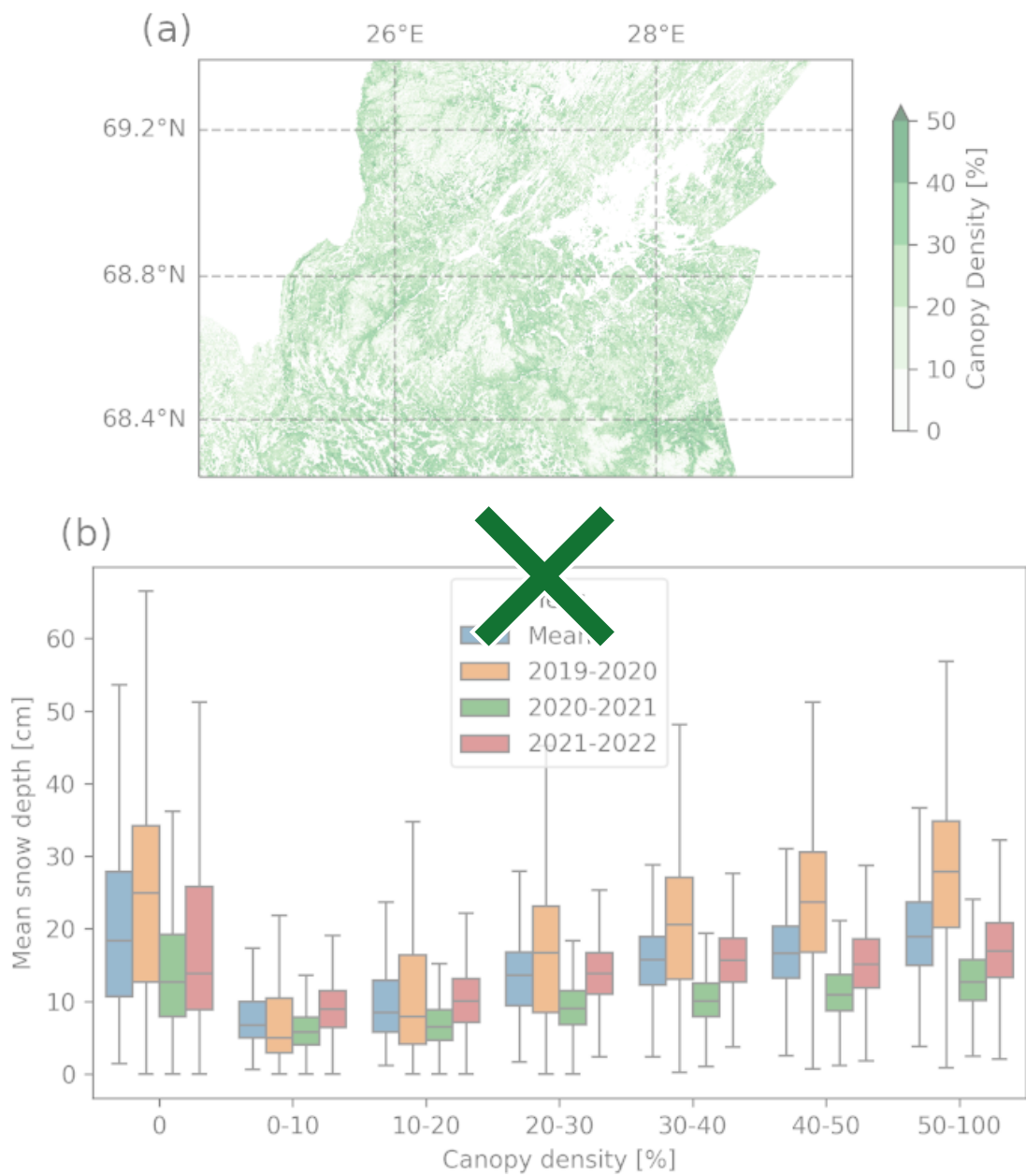
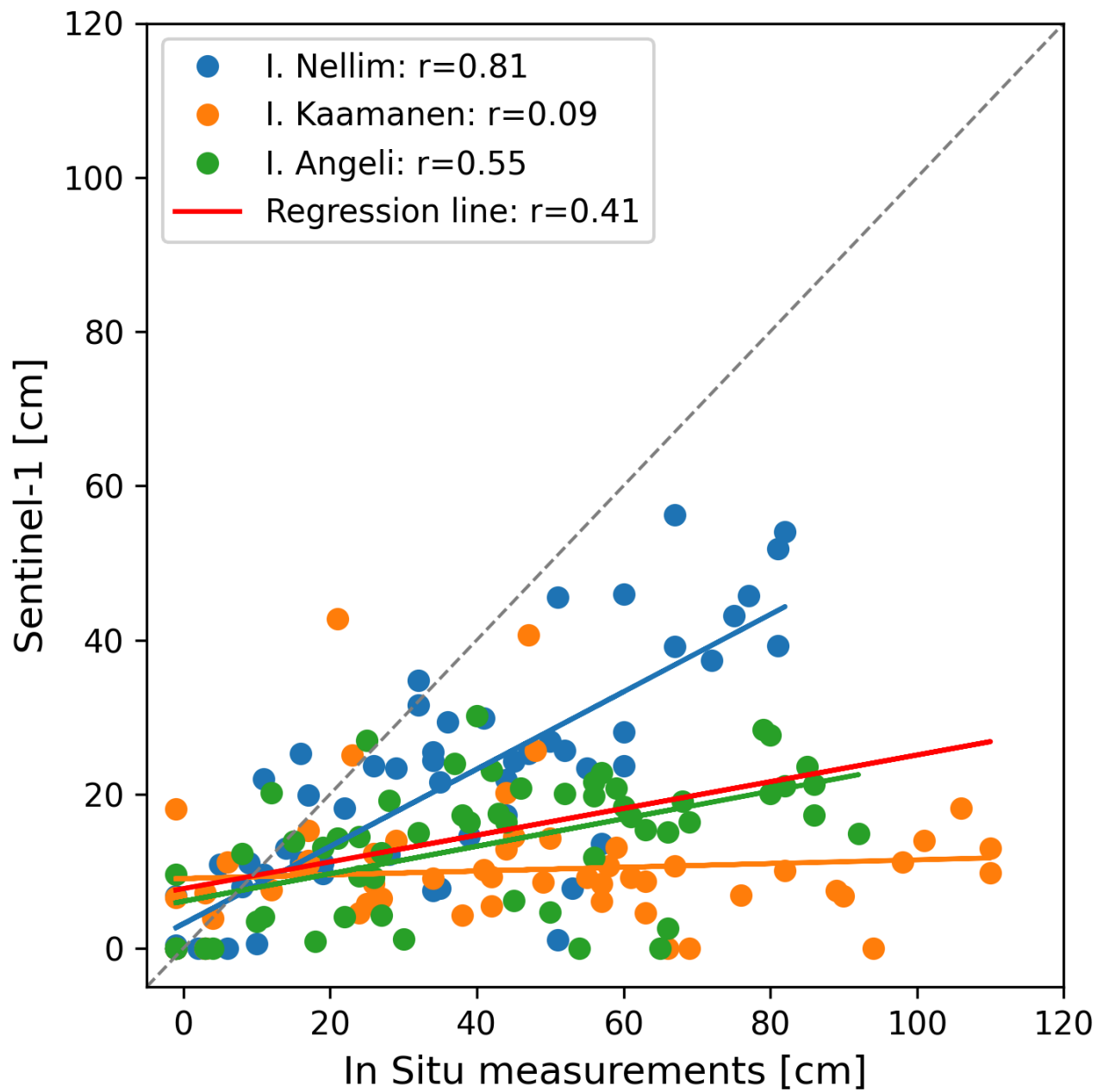
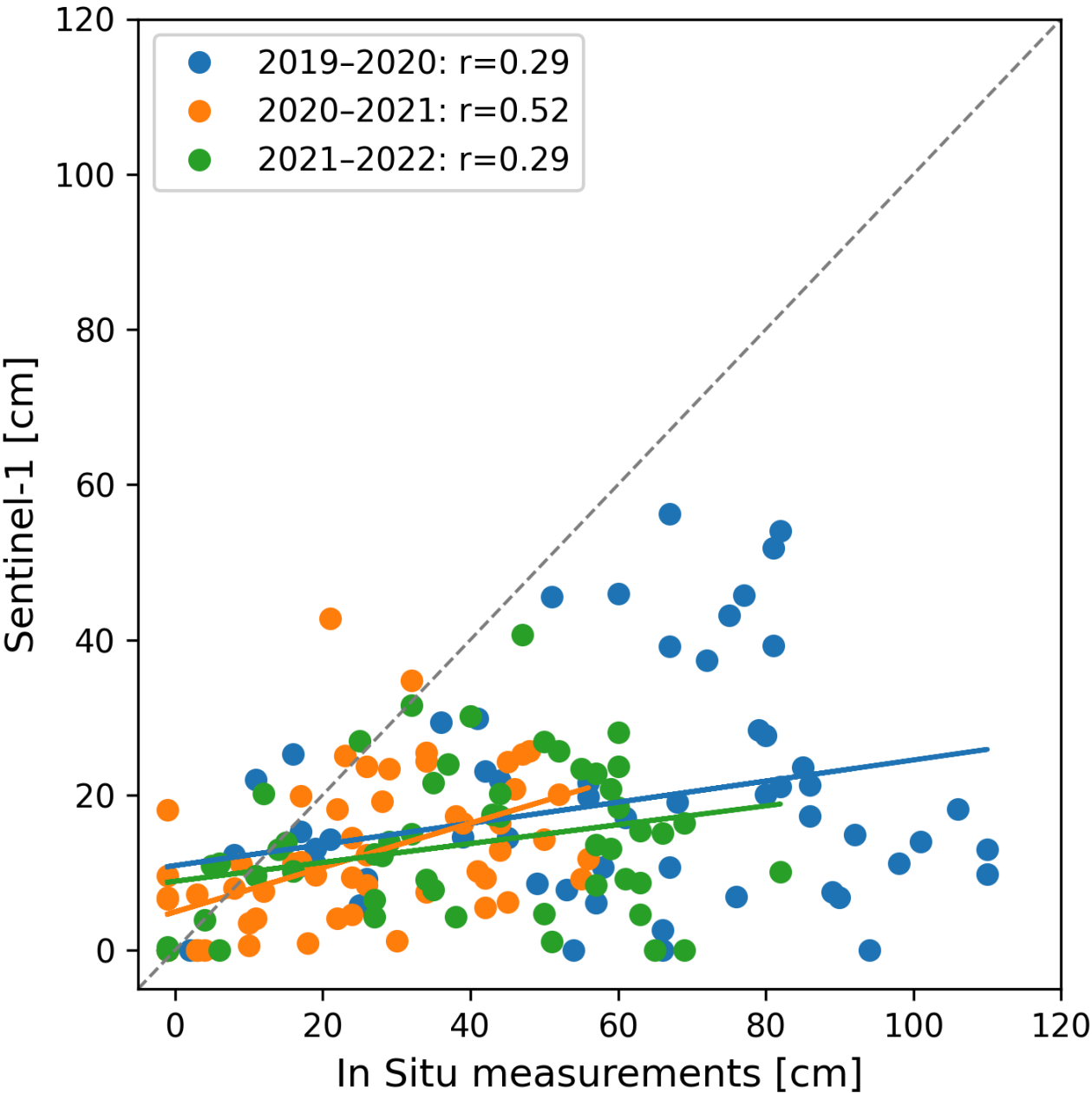


Figure 5: In situ measurements of snow depth compared to snow depth estimates derived from Sentinel-1. Different colours represent the different automatic weather stations, and the solid lines represent linear regressions of the dataset.



400
401

Figure 6: In situ measurements of snow depth compared to snow depth estimates derived from Sentinel-1. Different colours represent different years, and solid lines represent linear regression for each year.



404
405

Table 1: Mean snow depth values measured by the automatic weather stations (AWS), snow course measurements, and derived from the Sentinel-1 images separated by years.

408

	AWS mean (cm)				Sentinel-1 mean (cm)			
	2019-2020	2020-2021	2021-2022	2019-2022	2019-2020	2020-2021	2021-2022	2019-2022
IN	53.7 ± 1	22.1 ± 1	35.5 ± 1	37.1 ± 1	31 ± 16	13.7 ± 8	14.8 ± 8	20 ± 11
IK	70.9 ± 1	28.3 ± 1	41.6 ± 1	46.9 ± 1	8.5 ± 7	11.6 ± 6	10.2 ± 7	10.1 ± 7
IA	61.7 ± 1	28.1 ± 1	44.9 ± 1	44.9 ± 1	16.3 ± 12	8.8 ± 6	15.4 ± 9	13.4 ± 9
Overall	56.6 ± 1	22.4 ± 1	38 ± 1	39 ± 1	18.6 ± 12	11.3 ± 7	13.5 ± 8	14.5 ± 9
Snow Courses (cm)								
IN	57.3 ± 6	28.1 ± 3	45.0 ± 5	43.4 ± 5	45.8 ± 34	8.5 ± 9	5.7 ± 6	20.0 ± 16
IR	87.2 ± 10	52.5 ± 6	69.2 ± 8	69.6 ± 8	48.1 ± 25	16.8 ± 17	10.4 ± 10	25.1 ± 17
IL	91.8 ± 10	59.8 ± 7	68.7 ± 8	73.4 ± 8	24.6 ± 20	11.1 ± 11	16.0 ± 16	17.2 ± 16
IA	74.4 ± 8	39.6 ± 4	51.3 ± 6	55.1 ± 6	34.3 ± 56	23.9 ± 24	16.2 ± 16	24.8 ± 32
IM	67.1 ± 7	41.1 ± 5	38.0 ± 4	48.7 ± 5	47.6 ± 22	15.5 ± 15	11.3 ± 11	24.8 ± 16
IKa	93.3 ± 10	38.7 ± 4	49.4 ± 5	60.5 ± 7	9.8 ± 11	21.6 ± 22	18.6 ± 19	16.6 ± 17
Overall	78.5 ± 9	43.3 ± 5	53.6 ± 6	58.5 ± 6	35.0 ± 28.0	16.2 ± 16.2	13.0 ± 13.0	21.4 ± 19.1

409

	AWS mean (cm)				Sentinel-1 mean (cm)			
	2019-2020	2020-2021	2021-2022	2019-2022	2019-2020	2020-2021	2021-2022	2019-2022
Inari-Nellim (IN)	53.7±1	22.1±1	35.5±1	37.1±1	31.0±16	13.7±8	14.8±8	20.0±11
Inari-Kaamanen (IK)	70.9±1	28.3±1	41.6±1	46.9±1	8.5±7	11.6±6	10.2±7	10.1±7
Inari-Angeli Lintupuoliselkä (IA)	61.7±1	28.1±1	44.9±1	44.9±1	16.3±12	8.8±6	15.4±9	13.4±9
Overall	56.6±1	22.4±1	38.0±1	39.0±1	18.6±12	11.3±7	13.5±8	14.5±9

411

412

413 Table 2: Mean absolute error (MAE) and root mean square error (RMSE) separated by years.

	MAE (cm)	RMSE (cm)
2019-2020	38.9	48.6
2020-2021	14.0	18.7
2021-2022	25.5	32.7
2019-2022	26.1	35.6

414

